Chapter 4

Qualitative analysis of the core–surface fluid motions

«Τα πὰντα ρει και ουδὲν μὲνει»
Heracleitos

In this chapter I explore core–surface fluid motions which explain the temporal variation of the magnetic field at the CMB over the period 1980 – 2000. The non-uniqueness of this inverse problem is fundamental and was first recognized by Roberts & Scott [1965] and formalized by Backus [1968] leading to some assumptions to reduce the non-uniqueness of the geomagnetic core–surface motion problem. I will discuss the main assumptions, their shortcomings and the resulting fluid motion prediction. Furthermore I will highlight some geophysical implications for the Earth's angular momentum budget and geomagnetic jerks.

4.1 Inversion for core–surface flows

The secular variation of the magnetic field at a fixed point is characterized by two processes. First, there is a change in the field due to the advection of magnetic flux tubes by the fluid motion. Second, there is a diffusion of field lines relative to the motions due to ohmic dissipation. The induction equation for the magnetic field,

$$\partial_t \mathbf{B} = \nabla \times (\mathbf{u} \times \mathbf{B}) + \eta \nabla^2 \mathbf{B} , \tag{4.1}$$

with the condition

$$\nabla \cdot \mathbf{B} = 0 \tag{4.2}$$

describes how the time rate of change of the magnetic field $\mathbf{B}$ is due to these effects. $\mathbf{u}$ is the fluid velocity and $\eta = 1/(\mu\sigma)$ the magnetic diffusivity assumed uniform, with the magnetic permeability μ and σ the electrical conductivity of the core fluid. The first term of the right hand side (rhs) of the induction equation (4.1) represent the advection, the second term the diffusion of magnetic field lines. The ratio of transport to diffusion terms

in equation (4.1) is usually quantified by the magnetic Reynolds number R_m

$$\frac{|\nabla \times (\mathbf{u} \times \mathbf{B})|}{|\eta \nabla^2 \mathbf{B}|} \sim \frac{UL}{\eta} = R_m, \tag{4.3}$$

where U and L are characteristic velocity and length scales of the fluid motion, respectively. The length scales for advection and diffussion are assumed to be the same. With typical values ($L \simeq 10^6$ m, $U \simeq 5 \times 10^{-4}$ m s^{-1}, $\eta \simeq 1$ m^{2}s^{-1}) equation (4.3) gives that $R_m \approx 500$. Convection is apparently more important than diffusion. Alfvén [1942] suggested that diffusion could be neglected, the magnetic field being effectively frozen into the fluid. The magnetic field in a moving perfect conductor is governed by the diffusion-less induction equation

$$\partial_t \mathbf{B} = \nabla \times (\mathbf{u} \times \mathbf{B}) \tag{4.4}$$

With this condition, it can be shown that the frozen flux condition applies; the magnetic field is frozen within the fluid. The frozen–flux theorem and was first applied by Roberts & Scott [1965] to analyze the secular variation. They inverted the reduced equation for the flow at the core surface.

Now requiring that there is no fluid flow across the core–mantle boundary,

$$\mathsf{u_r} = 0 \left. \right|_{r=c} \tag{4.5}$$

and following the arguments of Backus [1968], then a further condition can be deduced which $\partial_t \mathsf{B_r}$ must satisfy if it is purely due to advection of $\mathsf{B_r}$ in a continuous velocity field $\mathbf{u}$ on the CMB:

If A is any patch on the CMB whose boundary ∂A is a null-flux curve ($\mathsf{B_r} = 0$ along this curve), then

$$\int_A \partial_t \mathsf{B_r} dA = 0 \,. \tag{4.6}$$

If either of these conditions fails, no continuous $\mathbf{u}$ will generate $\partial_t \mathsf{B_r}$ from $\mathsf{B_r}$, and flux diffusion must be invoked. From these conditions, Backus [1968] showed that, if there exists one (unique) $\mathbf{u}$ which satisfies (4.4), then there exist infinitively many. This is more obvious considering the radial diffusion–less induction equation

$$\begin{aligned}
\partial_t \mathsf{B_r} + \nabla_h \cdot (\mathbf{u}\mathsf{B_r}) &= 0 \\
\partial_t \mathsf{B_r} + \mathsf{B_r}\nabla_h \cdot \mathbf{u} + \mathbf{u} \cdot \nabla_h \mathsf{B_r} &= 0
\end{aligned} \tag{4.7}$$

where $\nabla_h = \nabla - \hat{r}(\hat{r} \cdot \nabla)$ is the horizontal divergence. A single equation (4.7) must be solved for two unknowns $\mathbf{u_h} = \{\mathsf{u}_\theta, \mathsf{u}_\phi\}$. The non–uniqueness can be reduced by imposing further constraint on the nature of the flow. Four different methods, which have been developed in the last two decades, are discussed in this chapter: steady flow, steady flow in an azimuthally drifting reference frame, tangentially geostrophic flow and flow caused by torsional oscillations. All these flow assumptions have in common a scheme of computation, which is outlined in the next section.

4.1.1 Scheme of the flow computation

The formalism of the flow calculation bases on a poloidal–toroidal decomposition of the velocity field as formulated by Roberts & Scott [1965]. Assuming $\nabla \cdot \mathbf{u} = 0$, the velocity field can be expressed in terms of two scalar functions of positions on the sphere, S and T. These functions can be expanded in spherical harmonics. So the decomposition reads

$$\mathbf{u} = \mathbf{u}_p + \mathbf{u}_t , \tag{4.8}$$

where

$$\begin{aligned}
\mathbf{u}_p &= \nabla_H(r\,S) = \left(0, \frac{\partial S}{\partial \theta}, \frac{1}{\sin \theta} \frac{\partial S}{\partial \phi} \right) \\
\mathbf{u}_t &= \nabla_H \times (\mathbf{r}\,T) = \left(0, \frac{1}{\sin \theta} \frac{\partial T}{\partial \phi}, -\frac{\partial T}{\partial \theta} \right) ,
\end{aligned} \tag{4.9}$$

are the poloidal and toroidal velocities and

$$\begin{aligned}
S(\theta, \phi) &= \sum_{l=1}^{\infty} \sum_{m=0}^{l} s_l^m Y_l^m(\theta, \phi) \\
T(\theta, \phi) &= \sum_{l=1}^{\infty} \sum_{m=0}^{l} t_l^m Y_l^m(\theta, \phi) .
\end{aligned} \tag{4.10}$$

Y_l^m is a real Schmidt quasi–normalized spherical harmonic. Substituting (4.8), (4.9), (4.10) into the rearranged radial induction equation (4.7)

$$\partial_t \mathsf{B_r} + \mathbf{u} \cdot \nabla_h \mathsf{B_r} + \mathsf{B_r} \nabla_h \cdot \mathbf{u} = 0$$

leads to a matrix equation

$$\dot{\mathsf{b}} = \mathbf{A}\mathsf{m} = \mathbf{E}\mathsf{t} + \mathbf{G}\mathsf{s} \tag{4.11}$$

which relates secular variation coefficients $\dot{\mathsf{b}} = \partial_t \mathsf{B} = \{\dot{g}_l^m, \dot{h}_l^m\}$ with toroidal and poloidal coefficients as model vector $\mathsf{m} = \{t_l^m, s_l^m\}$. The matrices $\mathbf{E}, \mathbf{G}$ are the Elsasser and Gaunt matrices. Following Bloxham [1988] the matrices have elements like

$$\begin{aligned}
E_{l_1 l_3}^{m_1 m_3} &= \frac{1}{4\pi c} \left(\frac{c}{a} \right)^{l_1+2} \frac{2l_1+1}{l_1+1} \sum_{l_2, m_2} \left(\frac{c}{a} \right)^{l_2+2} (l_2+1) g_{l_2}^{m_2} \\
&\times \oint \left(\frac{\partial Y_{l_3}^{m_3}}{\partial \theta} \frac{\partial Y_{l_2}^{m_2}}{\partial \phi} - \frac{\partial Y_{l_2}^{m_2}}{\partial \theta} \frac{\partial Y_{l_3}^{m_3}}{\partial \phi} \right) \frac{Y_{l_1}^{m_1}}{\sin \theta} dS \\
G_{l_1 l_3}^{m_1 m_3} &= \frac{1}{8\pi c} \left(\frac{c}{a} \right)^{l_1+2} \frac{2l_1+1}{l_1+1} \sum_{l_2, m_2} \left(\frac{c}{a} \right)^{l_2+2} (l_2+1)[l_1(l_1+1) + l_3(l_3+1) - l_2(l_2+1)] g_{l_2}^{m_2} \\
&\times \oint Y_{l_1}^{m_1} Y_{l_2}^{m_2} Y_{l_3}^{m_3} dS
\end{aligned}$$

These integrals are non–zero only for certain pairs of $(l_1, m_1), (l_2, m_2), (l_3, m_3)$ [Bullard & Gellman, 1954].

Equation (4.11) represents a linear inverse problem, $\partial_t \mathbf{B}$ and $\mathbf{B}$ are given in terms of Gauss coefficients, which were derived in the previous part of this study (chapter 3).

In the next sections I discuss some assumptions of how to relate the poloidal and toroidal velocities in order to solve equation (4.7) with less ambiguity for the core–surface flow.

4.1.2 Steady motion theorem

The idea first made by Gubbins [1982] that an unique solution could be derived by assuming the flow to be the same at three different times for a given point on the CMB was first formalized by Voorhies & Backus [1985]. Their approach as follows.

Suppose that for a given point on the CMB at three different times $\{t_i; i = 1, 2, 3\}$ $\mathsf{u_h}$ is the same, then three simultaneous equations for the unknowns $\mathsf{u}_\theta, \mathsf{u}_\phi, \partial \mathsf{u_r}/\partial r$ are given, namely

$$\partial_t \mathsf{B_r}(t_i) = \mathsf{B_r}(t_i)\frac{\partial \mathsf{u_r}}{\partial r} - \frac{1}{r}\frac{\partial \mathsf{B_r}(t_i)}{\partial \theta}\mathsf{u}_\theta - \frac{1}{r\sin\theta}\frac{\partial \mathsf{B_r}(t_i)}{\partial \phi}\mathsf{u}_\phi. \tag{4.12}$$

A unique solution exists, when the determinant is

$$\Delta = \hat{r} \cdot [\mathsf{B}_1(\mathsf{b}_2 \times \mathsf{b}_3) + \mathsf{B}_2(\mathsf{b}_3 \times \mathsf{b}_1) + \mathsf{B}_3(\mathsf{b}_1 \times \mathsf{b}_2)] \neq 0, \tag{4.13}$$

where $\mathsf{B}_i = \mathsf{B_r}(t_i), \mathsf{b}_i = \nabla_h \mathsf{B_r}(t_i)$ and $\dot{\mathsf{B}}_i = \partial_t \mathsf{B_r}(t_i)$ Then the solution is given by

$$\mathsf{u_h} = \Delta^{-1}\hat{r} \times \begin{vmatrix} \mathsf{b}_1 & \mathsf{b}_2 & \mathsf{b}_3 \\ \mathsf{B}_1 & \mathsf{B}_2 & \mathsf{B}_3 \\ \dot{\mathsf{B}}_1 & \dot{\mathsf{B}}_2 & \dot{\mathsf{B}}_3 \end{vmatrix}. \tag{4.14}$$

The condition $\Delta \neq 0$ reflects the fact that a minimal temporal variation of $\mathsf{B_r}$ is required to solve for the core-surface motion uniquely. Without this variability, even the assumption $\partial_t \mathsf{u_h} = 0$ does not permit $\mathsf{u_h}$ to be uniquely determined from magnetic measurements [Voorhies & Backus, 1985]. The immanent problem of the steady motion theorem is the fact that for short periods (some decades) applied the determinant Δ decreases and the three simultaneous equations become progressively less well conditioned, whereas applied for long periods (50 – 300 years) it does not recover rapid secular variation, i.e. geomagnetic jerks, at all. The conclusion is that time dependence of the flow is critical to the validity of the frozen flux hypothesis.

4.1.3 Steady flow in a azimuthally drifting reference frame

An extension of the steady flow assumption is the consideration of a steady flow in an azimuthally drifting reference frame. This approach, suggested by Voorhies & Backus [1985], and developed by Davis & Whaler [1996]; Holme & Whaler [2001] assumes the flow is steady in a frame fixed to the core, where the core frame is allowed to rotate with respect to the mantle about the Earth's rotation axis. The drift rate of this core frame might be

variable. For the remainder of this section, the primed variables are those of the drifting core frame.

Let

$$\psi = \phi - \phi', \tag{4.15}$$

where ψ is the accumulated drift angle. Then the flow as seen from the mantle frame is

$$\mathbf{u}(\theta, \phi, t) = \mathbf{u}'(\theta, \phi - \psi(t)) + r_c \frac{d\psi}{dt} \cos\theta \hat{\phi}, \tag{4.16}$$

where $\hat{\phi}$ is the azimuthal unit vector. Then

$$\partial_t \mathsf{B_r}' + \nabla_h(\mathbf{u_h}'\mathsf{B_r}') = 0 \tag{4.17}$$

is solved under the assumption of steady flow in the drifting core frame. Because of the Galilean invariance of $\mathbf{B}$ it must be the same whether in the stationary or drifting frame, so the Gauss coefficients in the drifting frame are

$$\begin{aligned}
g_l^{m'} &= g_l^m \cos m\psi + h_l^m \sin m\psi, \\
h_l^{m'} &= h_l^m \cos m\psi - g_l^m \sin m\psi.
\end{aligned} \tag{4.18}$$

The secular variation coefficients are

$$\begin{aligned}
\dot{g}_l^{m'} &= \dot{g}_l^m \cos m\psi + \dot{h}_l^m \sin m\psi + m\dot{\psi}h_l^{m'}, \\
\dot{h}_l^{m'} &= \dot{h}_l^m \cos m\psi - \dot{g}_l^m \sin m\psi - m\dot{\psi}g_l^{m'},
\end{aligned} \tag{4.19}$$

where the last term accounts for the relative velocity between mantle and core. Both transformations (4.18) and (4.19) are non–linear in drift angle Ψ.

Prescribed by the non–linearity of the transformation of the predicted $\dot{\mathsf{B}}_\mathsf{r}$ from the core to the mantle frame, the inversion is divided into two steps:

1.) The computation of the steady flow in the core frame. Here the flow velocity is represented as a linear combination of toroidal and poloidal vectors as outlined in section (4.1.1). The objective function to be minimized

$$\Theta(m) = (\mathsf{y} - \mathbf{A}\mathsf{m})^\mathsf{T}\mathbf{C_e}^{-1}(\mathsf{y} - \mathbf{A}\mathsf{m}) + \lambda_v \mathsf{m}^\mathsf{T}\mathbf{C_m}^{-1}\mathsf{m}, \tag{4.20}$$

where

$$\mathsf{m}^\mathsf{T}\mathbf{C_m}\mathsf{m} = \oint \left[(\nabla_h^2 \mathsf{u}_\theta)^2 + (\nabla_h^2 \mathsf{u}_\phi)^2 \right] dS = \sum_l \frac{l^3(l+1)^3}{2l+1} \sum_m [(t_l^m)^2 + (s_l^m)^2]. \tag{4.21}$$

λ_v is the damping parameter. Finally the solution for the model vector m is given by (3.24).

2.) The accumulated drift angle is parameterized as a function of time on the basis of cubic B–splines with 2.5 year knot spacing. Utilizing the cubic B–splines allows easy derivation of the drift rate $\dot{\psi}$ and the drift acceleration $\ddot{\psi}$.

The algorithm is set up to optimize for a set of spline coefficients which minimize the integral

$$\int_{t_1}^{t_2} \left[\int_{CMB} (\dot{\mathsf{B}_\mathsf{r}}^{obs} - \dot{\mathsf{B}_\mathsf{r}}^{pred}) dS + \lambda_d (\ddot{\psi})^2 \right] dt + \mathbf{C_m} \tag{4.22}$$

For each (non–linear) optimization step, to find the spline coefficients, the linear flow problem is solved. The non–linear optimization method applied here is the Powell's method to minimize a function of multiple variables [Press et al., 1993].

4.1.4 Geostrophic flow

This method follows from consideration of the force balance at the core–mantle boundary. Let us first consider the Navier–Stokes equation, which describes the forces acting in the viscous top layers of the core. The equation of motion and transfer of a viscous fluid in a rotating system reads

$$\rho \left(\frac{\partial \mathbf{u}}{\partial t} + (\mathbf{u} \cdot \nabla) \mathbf{u} \right) = -\nabla p + \rho \left(\rho' \mathbf{g} - 2 \mathbf{\Omega} \times \mathbf{u} - \mathbf{\Omega} \times (\mathbf{\Omega} \times r) + \mu \nabla^2 \mathbf{u} \right) + \mathbf{J} \times \mathbf{B} \tag{4.23}$$

where p is the non-hydrostatic part of the pressure, $\mathbf{g}$ gravitation, ρ the density, ρ' density fluctuation, $\mathbf{u}$ the fluid velocity, $\mathbf{\Omega}$ the Earth's angular velocity, μ the dynamic viscosity, $\mathbf{J}$ the current density and $\mathbf{B}$ the magnetic field. Suppose ρ is uniform and $\mathbf{g}$ is a conservative force, so that

$$\mathbf{g} = -\nabla \Phi \tag{4.24}$$

where Φ is the potential function[1]. The centrifugal terms can be rewritten by

$$\mathbf{\Omega} \times (\mathbf{\Omega} \times r) = -\nabla (\frac{1}{2} |\mathbf{\Omega} \times r|^2) \,, \tag{4.25}$$

then combining (4.24) and (4.25) gives an effective gravity $g_e = -\nabla(\Phi + \frac{1}{2} |\mathbf{\Omega} \times r|^2)$; then we can write (4.23)

$$\frac{\partial \mathbf{u}}{\partial t} + (\mathbf{u} \cdot \nabla) \mathbf{u} = -\frac{1}{\rho} \nabla p - 2 \mathbf{\Omega} \times \mathbf{u} + \nu \nabla^2 \mathbf{u} + \frac{1}{\rho} (\mathbf{J} \times \mathbf{B}) + \frac{\rho'}{\rho} g_e \tag{4.26}$$

where $\nu = \mu/\rho$ is the kinematic viscosity.

The geostrophic motion constraint, suggested by Hills [1979] and Le Mouël [1984] is based on the hypothesis that the Coriolis force balances the pressure gradient. This seems

---

[1]There are various sign conventions, I prefer to use the sign, that positive work is done against the potential.

to be justified, when all other forces compared with the Coriolis force are small:

$$\frac{\text{inertial force}}{\text{Coriolis force}} = \frac{|(\mathbf{u} \cdot \nabla)\mathbf{u}|}{|2(\mathbf{\Omega} \times \mathbf{u})|} \cong \frac{U}{2\Omega L \cos\theta} \cong 10^{-6}/\cos\theta, \tag{4.27}$$

$$\frac{\text{driving force}}{\text{Coriolis force}} = \frac{|\partial\mathbf{u}/\partial t|}{|2(\mathbf{\Omega} \times \mathbf{u})|} \cong \frac{1}{2\Omega T \cos\theta} \cong 10^{-5}/\cos\theta, \tag{4.28}$$

$$\frac{\text{viscous force}}{\text{Coriolis force}} = \frac{|\nu^2\nabla^2\mathbf{u}|}{|2(\mathbf{\Omega} \times \mathbf{u})|} \cong \frac{\nu}{2\Omega L^2 \cos\theta} \cong 10^{-15}/\cos\theta, \tag{4.29}$$

where $L = 10^6 \text{m}, U = 10^{-4}\text{ms}^{-1}$ (corresponding to a westward drift rate of $0.2°$ per year) and $T = 10^8\text{s}$. Estimations of the ratio of the Lorentz to Coriolis force are less simple, because only poloidal field is observable outside the core, whereas little is known about the toroidal field in the core–mantle boundary region. Every assessment of the ratio of the Lorentz and Coriolis force rely on the assumption that the toroidal field is weak and vanishes outside the core.

A lower bound for the poloidal field at the CMB is $B_p = 5 \cdot 10^{-4}T$. This value is given by a downward continuation of the observed magnetic field strength at the Earth's surface. For a purely poloidal field at the top of the core it is

$$\frac{\text{Lorentz force}}{\text{Coriolis force}} = \frac{|\mathbf{J} \times \mathbf{B_p}|}{|2\rho(\mathbf{\Omega} \times \mathbf{u})|} \cong \frac{B_p^2}{2\rho\Omega LU \cos\theta} \cong 10^{-3}/\cos\theta. \tag{4.30}$$

Then the flow in the top layers of the core is governed by this simplified equation of motion

$$-\frac{1}{\rho}\nabla p = 2(\mathbf{\Omega} \times \mathbf{u}), \tag{4.31}$$

$$\nabla \cdot \mathbf{u} = 0. \tag{4.32}$$

Equation 4.31 is known as the geostrophic flow equation and can be useful in approximating quasi-steady large-scale flow in the ocean, the atmosphere or even at the core–mantle boundary. An interesting result of the geostrophic flow equation is that the velocity field is found to be perpendicular to the pressure gradient.

The important result of the geostrophic flow approximation can be deduced by curling (4.31).

$$\nabla \times (2\mathbf{\Omega} \times \mathbf{u}) = -\frac{1}{\rho}\nabla \times (\nabla p) = 0. \tag{4.33}$$

Using the vector identity

$$\nabla \times (A \times B) = A\nabla \cdot B + (B \cdot \nabla)A - B\nabla \cdot A - (A \cdot \nabla)B$$

then the equation reads

$$\mathbf{\Omega}\nabla \cdot \mathbf{u} + (\mathbf{u} \cdot \nabla)\mathbf{\Omega} - \mathbf{u}(\nabla \cdot \mathbf{\Omega}) - (2\mathbf{\Omega} \cdot \nabla)\mathbf{u} = 0 \tag{4.34}$$

$\boldsymbol{\Omega}$ is independent of the position, so it follows

$$\boldsymbol{\Omega}\nabla \cdot \mathbf{u} - (\boldsymbol{\Omega} \cdot \nabla)\mathbf{u} = 0 \,. \tag{4.35}$$

Finally equation (4.32) gives

$$\boldsymbol{\Omega} \cdot \nabla \cdot \mathbf{u} = 0 \,. \tag{4.36}$$

By convention, the direction of $\boldsymbol{\Omega}$ is parallel to z

$$2\boldsymbol{\Omega}\nabla \cdot \mathbf{u} = 2\boldsymbol{\Omega}\frac{\partial \mathbf{u}}{\partial z} = 0 \rightarrow \frac{\partial \mathbf{u}}{\partial z} = 0 \,. \tag{4.37}$$

In words it means that in the absence of external forces the slow flow of a rotating, homogeneous, inviscid fluid is necessarily two–dimensional. The motion is confined to planes perpendicular to the axis of rotation. If the fluid is contained in a rigid spherical container, then the restriction on the motion is even more severe, the only slow motion possible are those in which cylindrical shells rotate like rigid bodies about the axis of rotation [Bullard & Gellman, 1954]. This result is known as Proudman–Taylor theorem [Proudman, 1916; Taylor, 1917], but was first derived by Hough [1897].

Now confining the flow in a horizontal plane to be geostrophic – no flow across the boundary

$$\mathsf{u_r} = 0 \,|_{r=c} \,, \tag{4.38}$$

then (4.31) reads

$$-\frac{1}{\rho}\nabla_h p = 2(\boldsymbol{\Omega} \times \mathbf{u})_h \,. \tag{4.39}$$

Multiplying (4.39) with r and taking the horizontal divergence yields the tangentially geostrophic constraint

$$\nabla_h(\mathbf{u}\cos\theta) = 0 \,. \tag{4.40}$$

The validity of (4.39) and therefore (4.40) breaks down at the geographical equator, where the pressure gradient cannot be balanced by Coriolis force any longer. Hence, the flow motion cannot be resolved uniquely. Backus & Le Mouël [1986] called this the leaky belt, but as pointed out by Chulliat & Hulot [2001] the non–uniqueness extend even to larger region than a equatorial band. The geostrophic regions can be defined as a set of points, where $|B_r/\cos\theta| \leq \zeta^2$. The value of ζ essentially depends on the radial derivative of the toroidal field (which is unknown), Chulliat & Hulot [2000] put a lower bound on $\zeta = 10^{-3}T$. The bright patches in figure 4.1 correspond to areas where the geostrophic assumption is expected to fail.

To construct solutions for (4.11) stochastic inversion (see section 3.4.2) is applied. The solution has to minimize the norm

$$\mathsf{m}^\mathsf{T} N_S \mathsf{m} = \oint \left[(\nabla_h^2 \mathsf{u}_\theta)^2 + (\nabla_h^2 \mathsf{u}_\phi)^2 \right] dS = \sum_l \frac{l^3(l+1)^3}{2l+1} \sum_m [(t_l^m)^2 + (s_l^m)^2] \,, \tag{4.41}$$

---

[2]Holme [priv. comm.] pointed out that flows perpendicular to the regions for which the geostrophic contours are closed are not resolved by tangential geostrophy.
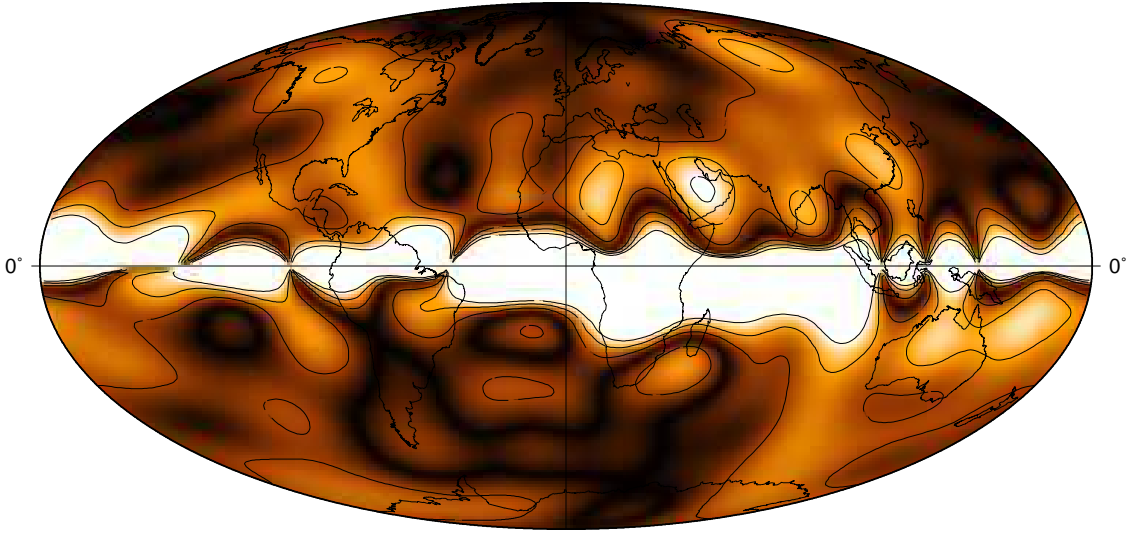
Figure 4.1: Sketch of the geostrophic degeneracy, the white region are the areas where the geostrophic assumption is expected to fail. ζ is chosen to be $10^{-3}T$.

i.e. the spatial roughness and the numerical convergence by the truncation degree of the velocity field at the CMB [Bloxham, 1988]. Further the solution should be smooth in time and minimizes

$$\mathsf{m}^\mathsf{T} N_T \mathsf{m} = \oint \left(\frac{\partial \mathbf{u}}{\partial t} \right)^2 dS = \sum_l \frac{l(l+1)}{2l+1} \sum_m [t_l^m + s_l^m]^2 \,. \tag{4.42}$$

The flow is also forced to be close to tangential geostrophic and therefore to minimize the quantity

$$\mathsf{m}^\mathsf{T} N_G \mathsf{m} = \oint \left[\nabla_h \cdot (\mathbf{u} \cos(\theta)) \right]^2 dS \,. \tag{4.43}$$

All three norms can be expressed as quadratic form

$$\mathsf{m}^\mathsf{T} \mathbf{C_m}^{-1} \mathsf{m} = \lambda_s N_S^{-1} + \lambda_t N_T^{-1} + \lambda_g N_G^{-1} \,, \tag{4.44}$$

which gives the formal solution

$$\mathsf{m} = (\mathbf{A}^\mathsf{T} \mathbf{C_e}^{-1} \mathbf{A} + \mathbf{C_m})^{-1} \mathbf{A}^\mathsf{T} \mathbf{C_e}^{-1} \dot{\mathsf{b}} \tag{4.45}$$

that minimizes an objective function similar to (3.25). The results of the flow inversion are discussed in section (4.2).

4.1.5 Torsional oscillation

It has been suggested that an observed variation of the magnetic field with a period of ≈ 60 years may be related to torsional oscillations of rigid cylindrical surfaces aligned with the rotation axis [Braginskii, 1970, 1984].

The last section provided the dynamical description on cylindrical surfaces leading now to an analysis of these oscilations around an quasi–equilibrium state, the so–called Taylor state.

Taylor [1963] considered the steady ($\partial/\partial t = 0$), slow motion of an inviscid fluid ($\nu = 0$), then the force balance reads

$$2\mathbf{\Omega} \times \mathbf{u} = -\frac{1}{\rho}\nabla p + \frac{1}{\rho}(\mathbf{J} \times \mathbf{B}) + \frac{\rho'}{\rho}g_e \,. \tag{4.46}$$

When integrated azimuthally over a cylindrical surface (4.46) reduces to

$$2\mathbf{\Omega} \int_{\Sigma} (\mathbf{u})_\phi d\Sigma = \int_{\Sigma} (j \times \mathbf{B})_\phi d\Sigma \tag{4.47}$$

with $d\Sigma = sd\phi dz$ and (s, ϕ, z) the cylindrical coordinates. The buoyancy force $\frac{\rho'}{\rho}g_e$ is equal to zero, because it acts only in meridional planes and has therefore no azimuthal component. The azimuthally integrated component of the pressure gradient force is also zero. Because of the continuity equation

$$\nabla \cdot \mathbf{u} = 0 \tag{4.48}$$

the left hand side of (4.47) is equal to zero

$$\int_{\Sigma} \mathbf{u}d\Sigma + \int_{N(s)} \mathbf{u}dS + \int_{S(s)} \mathbf{u}dS = \int \nabla \cdot \mathbf{u}dV = 0 \,, \tag{4.49}$$

where $N(s)$ and $S(s)$ are the spherical caps of the cylinder as shown in figure (4.2) [Gubbins & Roberts, 1987]. There is no net–flow out or into the cylinder. Finally it remains

$$\int_{\Sigma} (\mathbf{J} \times \mathbf{B})_\phi d\Sigma = 0 \,, \tag{4.50}$$

In order to have a velocity $\mathbf{u}$ compatible with (4.1), (4.46) and (4.48), then it is necessary for the magnetic field of a slow and inviscid rotating fluid in a rigid spherical geometry to satisfy (4.50). This is Taylor's constraint. A further implication of (4.50) is, that the coupling between the annular cylinders co–axial with the rotation axis must vanish. Recent studies suggest that the geodynamo is currently oscillating around its Taylor state [Zatman & Bloxham, 1997, 1998; Bloxham et al., 2002], where the azimuthal components of the Lorentz force integrated over the cylinder surface vanishes, except the part involved in torsional oscillation. In order to excite torsional oscillation the geodynamo must have departed from its Taylor state. Jault & Le Mouël [1989]; Jault et al. [1996] showed that topographic and gravitational coupling[3] between the core and the mantle lead to this departure from the Taylor state and excite motions in cylindrical annuli of the type

$$\mathbf{u}_G = \mathbf{u}_\phi(s)\hat{\phi} \,. \tag{4.51}$$
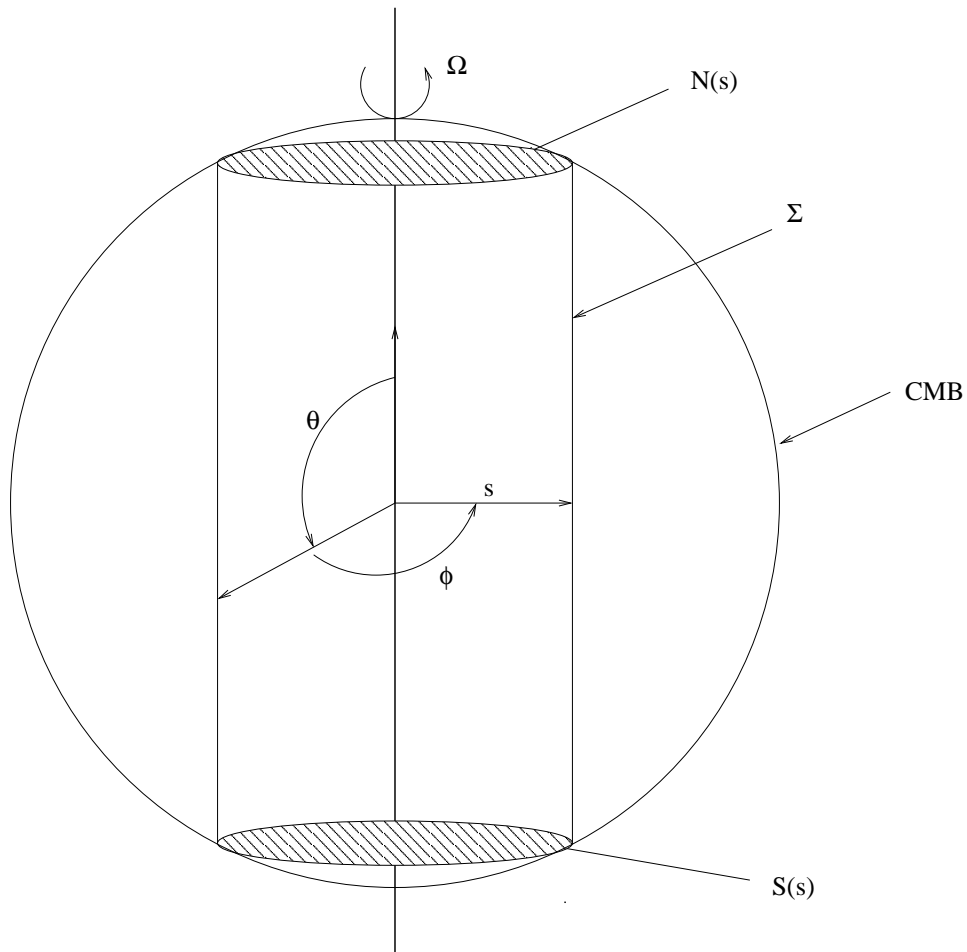
Figure 4.2: Sketch of the core geometry to illustrate the Taylor constraint

The fluid motion (4.51) will distort the magnetic field lines, causing a curvature to the field lines. The curvature generates a Lorentz force on the fluid which counteracts further curvature as predicted by Lenz's law and reverses the direction of the fluid flow. The field lines return to the undistorted configuration and beyond until the Lorentz force becomes strong enough again to stop fluid motion and to reverse it. Once the oscillations are initiated, they are unaffected by the toroidal field, and only the component perpendicular to the rotation axis, B_s, determines the restoring force and the period of torsional oscillation. A range of periods between 60 years [Braginskii, 1970] and 25 years [Gubbins & Roberts,

---

[3]Topographical coupling is due to dynamical pressure variation acting on an aspherical CMB [Hide, 1969], whereas gravitational coupling is due to the action of an aspherical geoid acting on density inhomogeneities in the core.
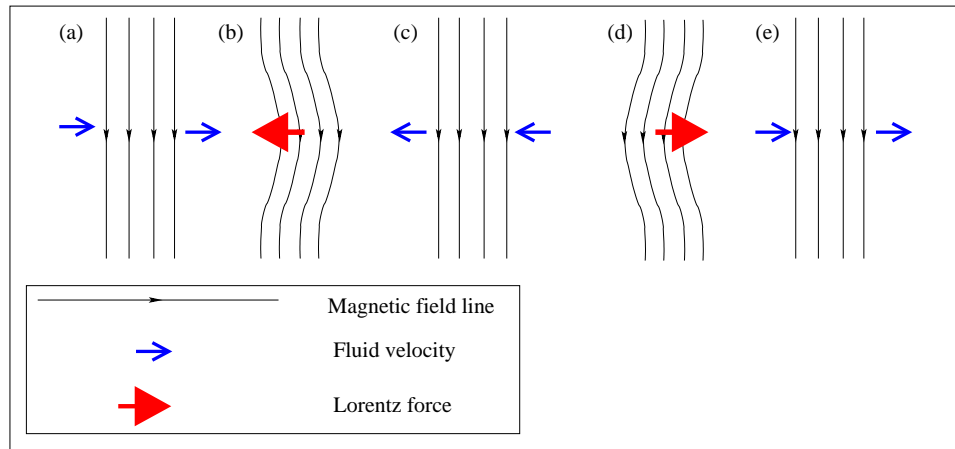
Figure 4.3: Figure shows the excitation mechanism of Alfvén like waves, such as torsional oscillation. Courtesy of C. Finlay

1987] has been suggested depending on the assumed strength of B_s in

$$T \simeq \frac{2\mu_0 \rho \lambda}{B_s^2} \tag{4.52}$$

where λ is the wavelength, $B_s = 5\text{mT}$[Gubbins & Roberts, 1987]. Without ohmic dissipation or viscosity these oscillations are undamped. Figure (4.3) depicts a complete cycle of the action due to the competing inertial force and Lorentz force [Finlay, 2004a].

The method of inversion for the flow motion is basically the same as outlined in section 4.1.4, the only distinction between these methods is the temporal damping of the toroidal components of the flow. Here the temporal damping of these components is relaxed and therefore the toroidal flow can more vary with time. Compared with Zatman & Bloxham [1997, 1998] and Bloxham et al. [2002] this approach is more general, but should recover the same behaviour of the fluid flow.

4.2 Maps of core–surface flows

In this section I compare the resulting flows derived using the different constraints outlined in the previous sections. First, I consider the maps based on the steady flow assumption and its extension in a azimuthally drifting reference frame, then the flows which based on tangential geostrophy are presented.

4.2.1 Steady flows

The steady flow for a single epoch was derived from triplets of the secular variation and the main field of the center epoch, i.e. 1990, and the adjacent epochs separated by five years, i.e 1985 and 1995. The figure 4.4 show the steady flows centering on the epochs 1985, 1990 and 1995. Similarities and differences are evident, all graphs show a pronounced westward drift. All figures show flows across the equator, most clearly around 1985 and 1995 near South America and 1985 near Indonesia. In at least two of the figures, namely for 1990 and 1995, a big circulation is apparent southeast of Africa. Also a strong circulation seems to have existed in 1985 underneath Indonesia. This gyre is less clearly defined in 1990 and has disappeared in 1995.
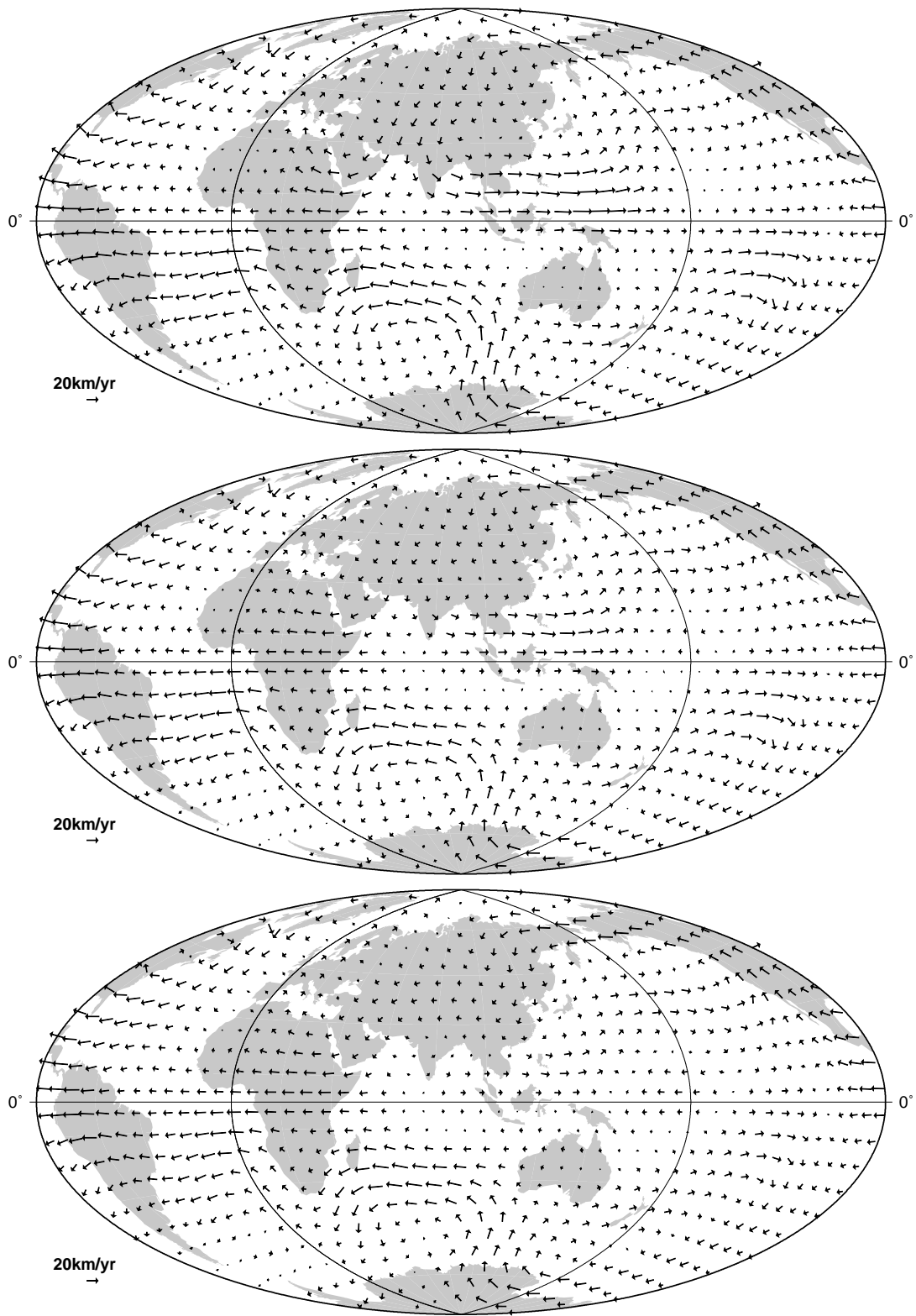
Figure 4.4: Steady flows centered on 1985, 1990 and 1995. The vectors show the velocity and direction of the fluid motion at the CMB.

4.2.2   Steady flows in an azimuthally drifting reference frame

The first finding of the examination of solutions for different damping parameters λ_v is shown in figure 4.5. The curves of the objective function differ for different λ_v. The minimum for strong damping coincide with a drift rate of approximately -10 km/yr, which is in a good agreement with the known value of the westward drift. Two further minima appear, when the damping is relaxed. One for -60 km/yr and an other for 49 km/yr, what would correspond to a westward drift and eastward drift, respectively. The appearance
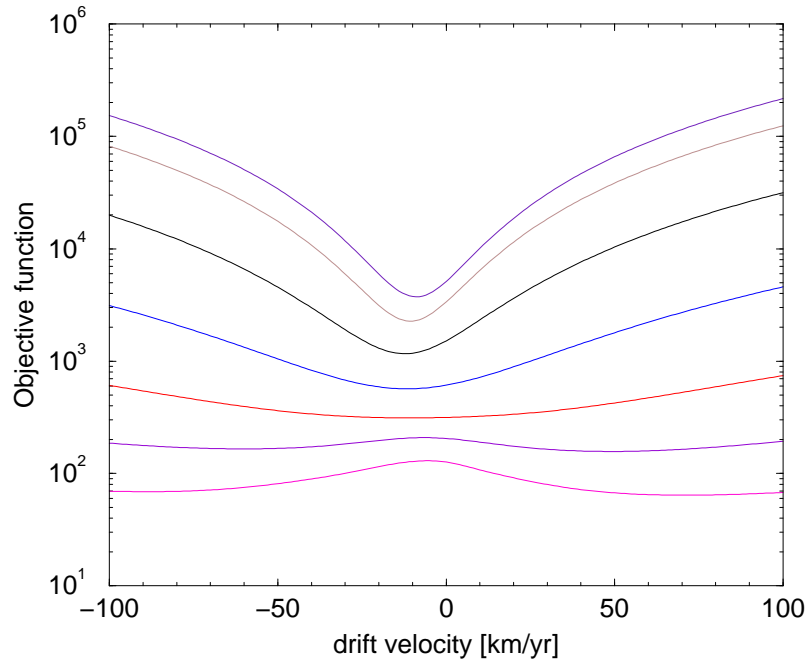
Figure 4.5: Objective function as a function of drift rate for different damping parameters λ_v.

of two solutions for the drift rate, when the damping is relaxed, is not comprehendible at once. In fact Holme & Whaler [2001] argued that the two solutions are caused by flows drifting with nearly equal and opposite angular velocity so that

$$\mathbf{u}_1(\theta, \phi, t) = \mathbf{u}'(\theta, \phi - \psi(t)) + r_c \frac{d\psi}{dt} \cos\theta \hat{\phi}$$

$$\mathbf{u}_2(\theta, \phi, t) = \mathbf{u}''(\theta, \phi + \psi(t)) - r_c \frac{d\psi}{dt} \cos\theta \hat{\phi}.$$

Any linear combination of the two flows will explain the secular variation. Possible scenarios could be that both flows represent two traveling waves making up a standing wave. But also two convection rolls, as inferred from the maps of the radial magnetic field (figure 3.7) in opponent rotation would give a possible explanation.

Three solutions were constructed for three uniform drift rates: one eastward centered on 49.0 km/yr and two westward centered on -10.81 or -60.0 km/yr, respectively. These three drift velocities correspond to the three minima found for the objective function (see figure 4.5). The diagnostics for the three flow solutions are given in table 4.1. The flows with the higher drift velocities tend to be more energetic than the one with the drift speed centered on -10.81 km/yr, also the fit of the slow drifting flow to the secular variation is poorer than for the two fast drifting flows. Figure C.1 shows the comparison of the first 18 secular variation coefficients from the time–dependent model and predicted by the three flow solutions. All three solutions show a distinct temporal behaviour, but have in common that the recovering of the short term secular variation is rather poor. In figure 4.6 maps

	W Drift (W1)	W Drift (W2)	E Drift (E1)
drift velocity (km/yr)	-10.81	-60.0	49.0
rms secular variation misfit (nT/yr)	4.43	2.91	2.77

Table 4.1: Diagnostics of the drifting flow.

of the drifting flow solution for weak damping and eastward drift is shown. The three top graphics represent snapshots for three different times (1980, 1990 and 2000) as observed in the mantle frame. These flows do not significantly from those of the steady flow (cf figure 4.4). The bottom graphic shows the flow as seen in the drifting frame, here the flow is dominated by the strong eastward drift of about 49 km/yr.
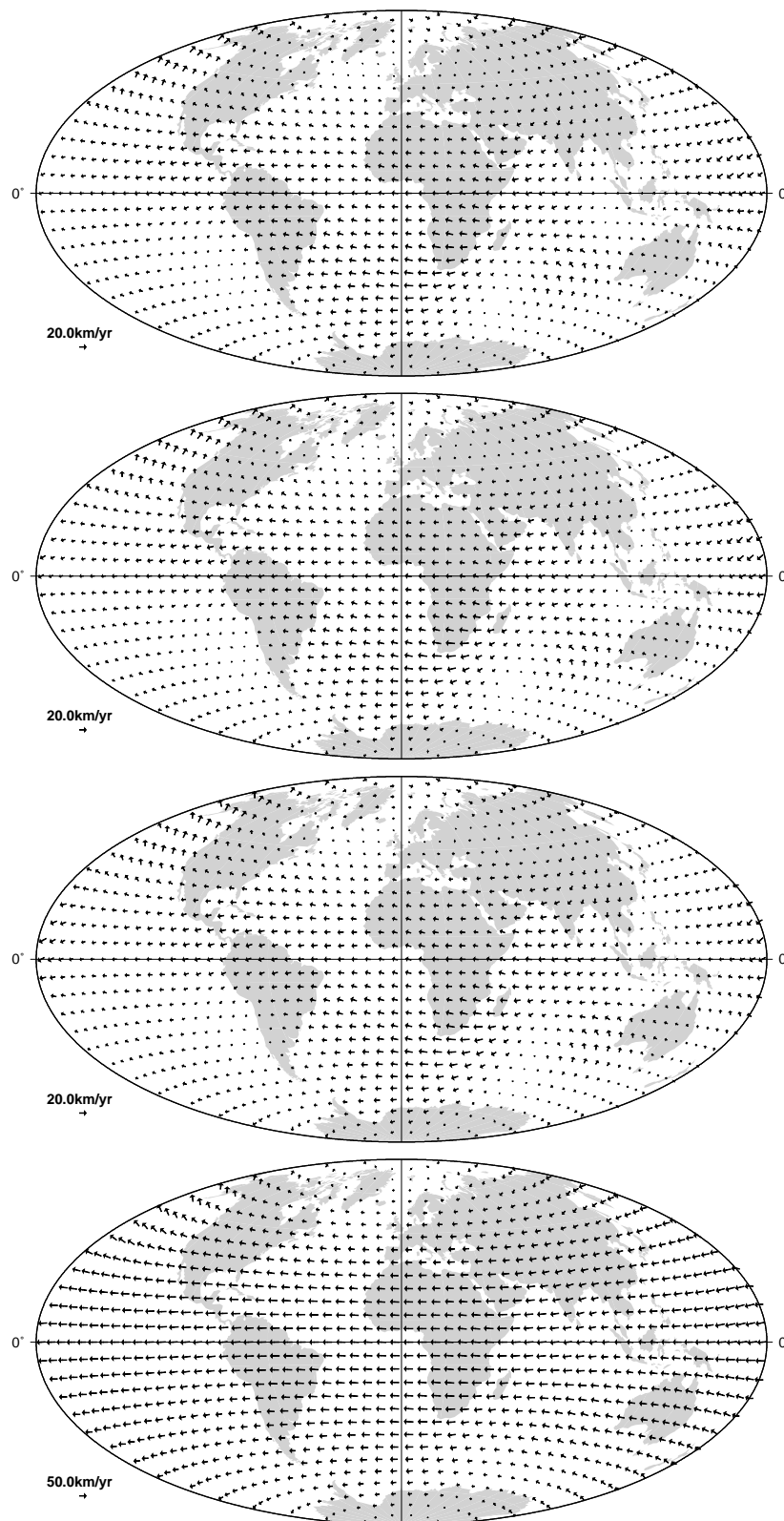
Figure 4.6: The three top maps show the drifting flows for 1980, 1990, and 2000 in the mantle frame. The bottom map shows the steady flow in the drifting reference frame.

4.2.3   Tangetially geostrophic flows and torsional oscillation

The solution is found as the knee point in the trade off curves between the averaged velocity of the flow and the secular variation misfit, as shown in figure 4.7. The trade off curves show very weak dependence of the temporal damping; therefore, the curves for strong $\lambda_t = 0.1\text{E}+03$, medium $\lambda_t = 0.1\text{E}-01$ and weak $\lambda_t = 0.1\text{E}-09$ temporal damping overlay. The preferred solution is obtained for strong temporal and geostrophic constrains
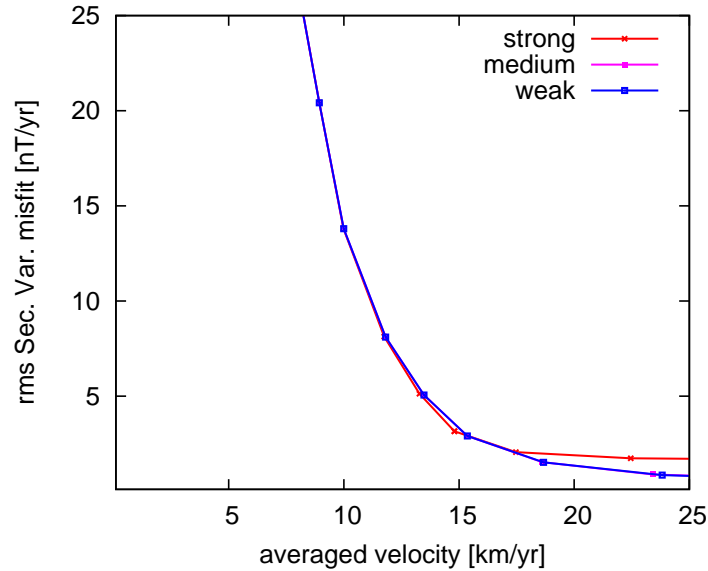
Figure 4.7: Trade off curves for three different temporal damping: strong $\lambda_t = 0.1\text{E}+03$, medium $\lambda_t = 0.1\text{E}-01$ and weak $\lambda_t = 0.1\text{E}-09$.

and referred to as flow 1 for the remainder of this study. Figure 4.8 shows the flow 1 for three different epochs.

The dominant features are a strong circulation southeast of Africa, a strong clockwise circulation centered underneath Labrador, strong westward directed flow in equatorial regions and weak flow in the Pacific region. The circulation centered southeast of Africa shows a rather complex structure and seems to be linked to a smaller gyre under the south Atlantic. Both gyres are parts of a much larger pattern in the southern hemisphere, which appears as a bending wave starting in east Antarctica and fades out across the south Pacific. All features are persistent during the 20 years interval. The ratio of the energy density of the equatorial symmetric and asymmetric flow components is 2.8; the flow is strongly equator symmetric.

The assumption of frozen flux and tangential geostrophy determine up and downwelling by

$$\nabla_h \cdot \mathbf{u_h} = \frac{\tan(\theta)}{c} \, \mathsf{u}_\theta \,. \tag{4.53}$$

		Flow 1	Flow 2	Flow 3
Damping	spatial λ_s	2.0×10^{-4}	2.0×10^{-4}	2.0×10^{-4}
	temporal λ_t	1.0	1.0	1.0
	temporal λ_{tz} (for zonal terms)	-	-	$\times10^{-3}$
Diagnostic	geostrophic norm	4.80×10^{-2}	220.09	4.80×10^{-2}
	spatial smoothness norm	15.57×10^6	1.01×10^6	15.57×10^6
	temporal smoothness norm	103.6	152.35	97.93
	time averaged velocity (km/yr)	15.33	11.44	15.33
	time averaged acceleration (km/yr^2)	2.87	3.48	2.90
	characteristic flow time (years)	5.34	3.28	5.28
	rms secular variation misfit (nT/yr)	0.80	1.49	2.91
	rms ang. mom. misfit	2.04	4.83	2.08

Table 4.2: Parameters and diagnostics of the inversions for two tangentially geostrophic flow and the flow invoking torsional oscillation.

Fluid up and downwelling is depicted in a color scale. This description seems to be insensitive for greater latitude and regions of fluid up and downwelling concentrate near the equator, where the geostrophic assumption is supposed to fail and therefore the magnitude of the upwelling cannot be given with high confidence. Nevertheless, it is worth noting that the strongest fluid up and down welling coincide with the regions, where the column rolls are expected from the analysis of the morphology of the radial field at the CMB (section 3.5.1).

Fluid upwelling is also to see in connection with magnetic diffusion, because the toroidal field is advected by fluid upwelling as sketched in figure 4.9. Upwelling results in a field concentration which is then twisted by a vertical velocity field. Finally, reconnection leads to magnetic diffusion of the field through the CMB.

As already mentioned, constraining the flow temporally does not have a significant effect on the solution itself, rather the tangentially geostrophic constraint controls the flow. Therefore a second solution, flow 2, is analysed, where the geostrophic constraint is relaxed by ten orders of magnitude. Relaxing the geostrophic constraint lets the ageostrophic part in the flow solution rise. Ageostrophy occurs, when the balance between pressure gradient and the Coriolis force is deranged. A perfect geostrophic balance would mean that the fluid motion is along lines of constant pressure, implicitly assuming that the tangential velocity with respect to the boundary is zero (4.38). This can only be achieved, when a thin viscous layer exists, the Ekman layer. The frictional drag F within this layer unbalances the geostrophic flow and generates an ageostrophic flow

$$2\mathbf{\Omega} \times \mathbf{u}_{ag} = F\,. \tag{4.54}$$

The imbalance deflects the flow towards lower pressure[4]. See figure 4.10. The maximum

---

[4]This phenomenon is also known from the Earth's atmosphere, where the geostrophic wind feels the frictional drag of the rough underlying surface.

ageostrophic velocity never exceeds 3 km/yr, is strongest in the region of the geostrophic degeneracy (see figure 4.1) and crossing the equator. The direction of the friction, which can be deduced from this graph, is more or less symmetric to the equator and pointing either west or east.

A third flow solution (flow 3) is analysed, where only zonal components of the flow are allowed to vary with time. The maps of the torsional oscillation flow are shown in figure 4.12. The difference to flow 1 is insignificant. For comparison of the inversion parameters and characteristics of all three flows, see table 4.2. The results of an analysis of the time averaged velocity field is given in the table (4.3).

	Flow 1	Flow 2	Flow 3
total flow kinetic energy	210.90	145.97	210.96
toroidal component[1]	94.49	83.94	94.48
poloidal component[1]	5.51	16.06	5.52
symmetric component[1]	66.39	71.25	66.39
symmetric toroidal component[2]	98.73	89.93	98.73
symmetric poloidal component[2]	1.27	10.07	1.27
asymmetric component[1]	33.61	28.75	33.61
asymmetric toroidal component[3]	86.13	69.08	86.10
asymmetric poloidal component[3]	13.87	30.92	13.90
geostrophic component[1]	99.96	75.05	99.96
ageostrophic component[1]	0.03	24.94	0.03
zonal toroidal component[1]	16.12	38.22	16.13

Table 4.3: Characteristics of the two tangentially geostrophic flows and the flow invoking torsional oscillation. The total energy is given in arbitrary units and the components as percentage of the total flow (1) and the total symmetric component (2) and total asymmetric component (3), respectively.
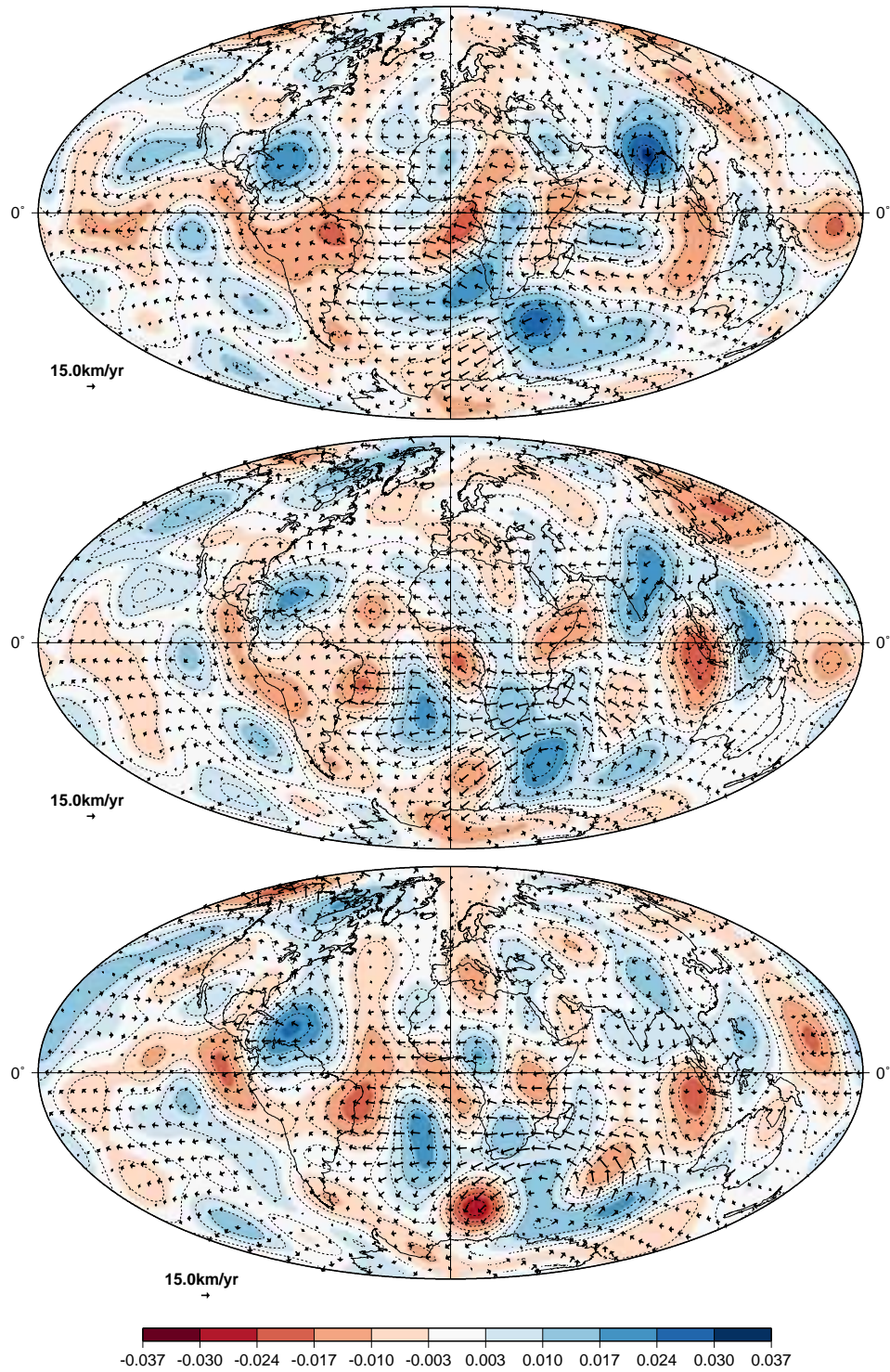
Figure 4.8: Tangentially geostrophic flows for 1980, 1990 and 2000. The vectors show the velocity and direction of the fluid motion at the CMB. The color scale shows the intensity of the horizontal divergence (upwelling and downwelling) of the flow.
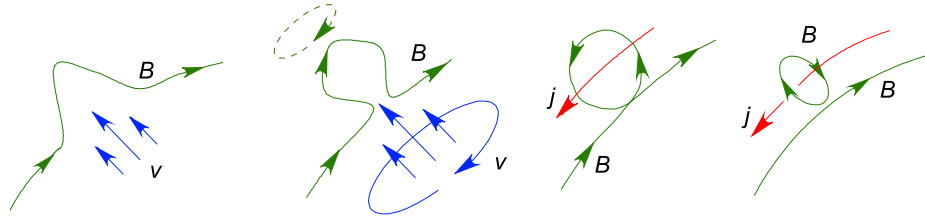
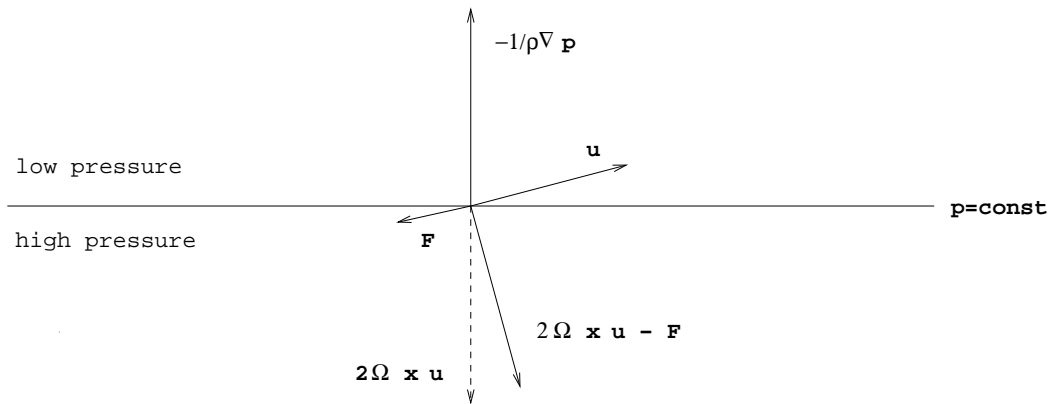Figure 4.9: Sketch of the toroidal flux expulsion in an electrically conducting medium.

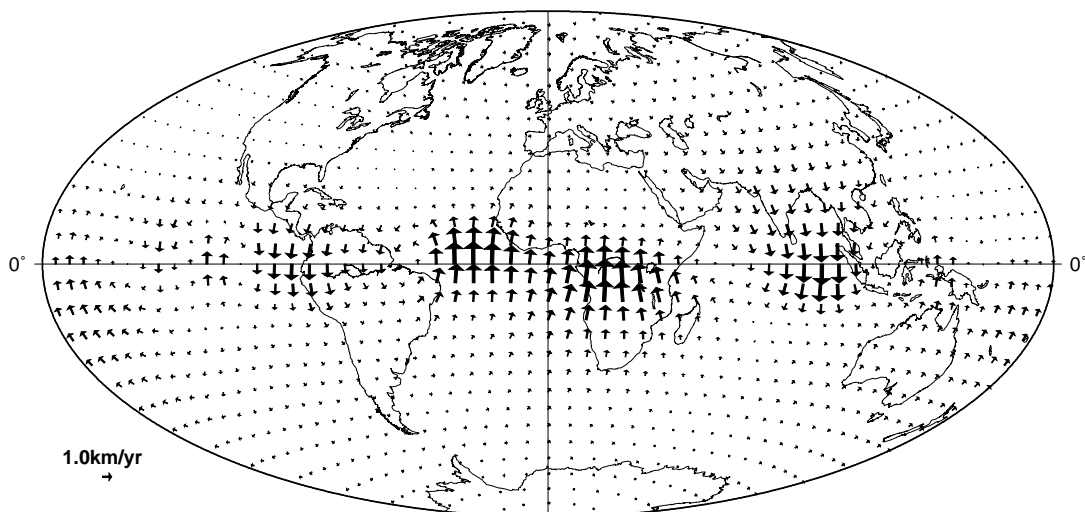Figure 4.10: The ageostrophic force balance, where F is the frictional drag.
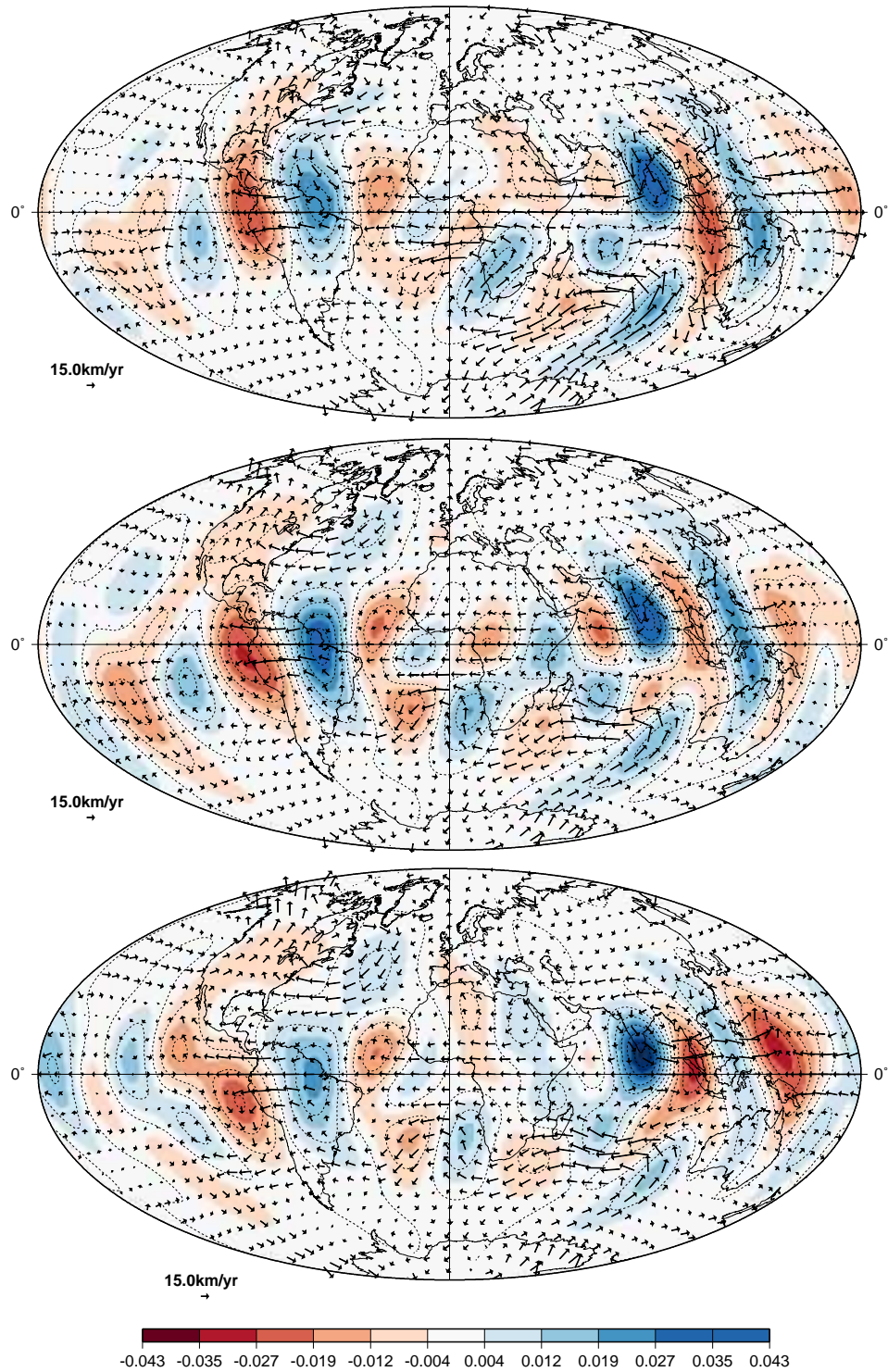

Figure 4.11: The ageostrophic part of the flow 2.

Figure 4.12: Torsional oscillation flows (flow 3) for 1980, 1990, and 2000. The vectors show the velocity and direction of the fluid motion at the CMB.

Like in chapter 3 a resolution analysis of the solutions is carried out. In figure 4.13 the resolution of the toroidal (left) and the poloidal velocity coefficients (right) are shown. The resolution is derived at the six times during 1980 and 2000. The resolution of the flow inversion is fairly time invariant, as the six curves overlay. Recalling, that low resolution means the model is controlled by the regularization or a priori beliefs, whereas high resolution states that the model is controlled by the data, i.e. the model for secular variation and the main field. The resolutions for toroidal and poloidal terms differ significantly, for the toroidal terms it is higher than for the poloidal ones. This appears to be expected from point of view, that the poloidal flow is more constrained by applying the tangentially geostrophic constraint. It becomes immediately clear, when considering the resolution of less tangential geostrophic constrained solution (figure 4.14). Here the resolution of the poloidal terms (right panel) is of the order of the resolution of the toroidal terms (left panel).
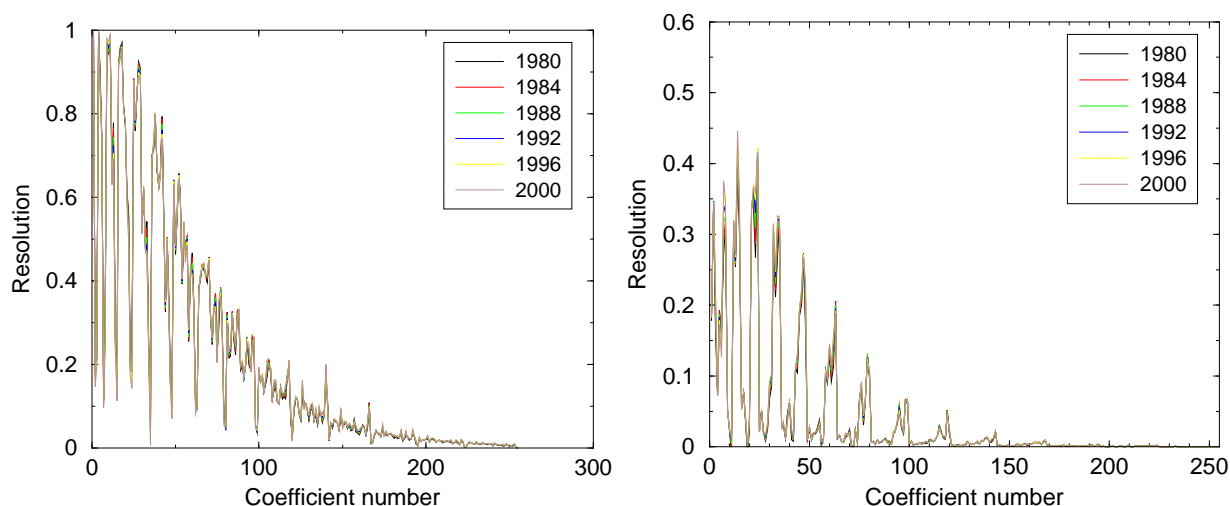

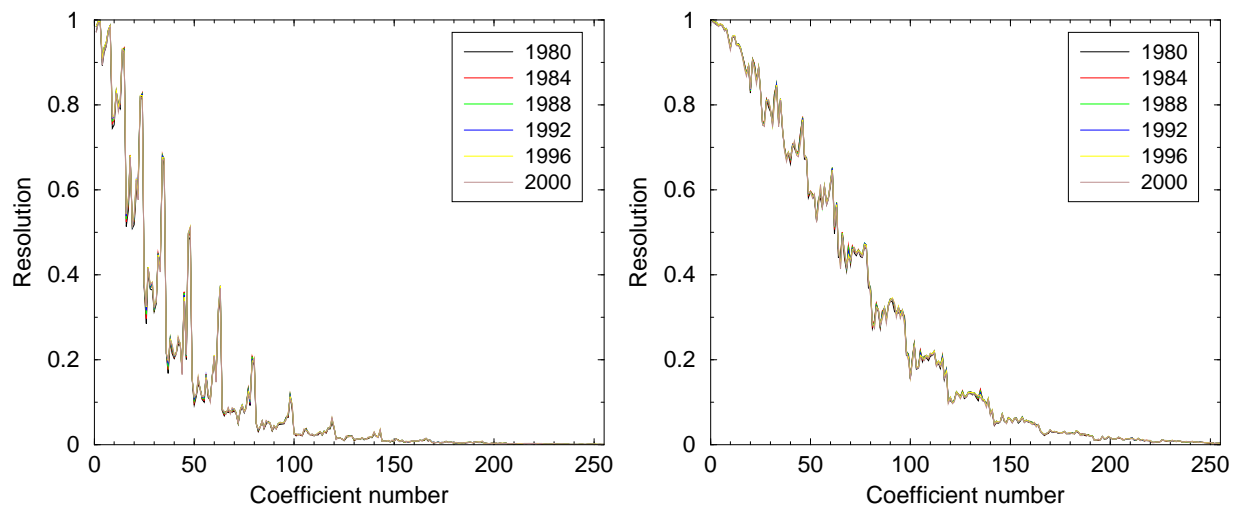Figure 4.13: The resolution of the toroidal (left) and poloidal velocity coefficients (right) for flow 1.

Figure 4.14: The resolution of the toroidal (left) and poloidal velocity coefficients (right) for flow 2.

4.2.4   Prediction of secular variation from flows

Figure 4.15 provides the fit of the secular variation predicted by different flow assumptions to that of the time–dependent model derived in the previous chapter. The overall impression is that flow 1, 2 and 3 recover the secular variation at all chosen stations fairly good. Table 4.2

The predictions by the drifting flow is rather poor. It captures only the gross features of the secular variation, but cannot account for the short term variation, i.e. jerks. However, this fact may help to evaluate possible explanation for geomagnetic jerks. The incapacity of the drifting flow to fit short term secular variation allows to different scenarios for the generation of short term secular variation: either jerks are related to flux expulsion or caused by non–equator symmetric flows.

I also tested the hypothesis if the secular variation can be attributed to a flow which is purely toroidal. This means that equation 4.7

$$\partial_t \mathsf{B_r} + \mathsf{B_r}\nabla_h \cdot \mathbf{u} + \mathbf{u} \cdot \nabla_h \mathsf{B_r} = 0$$

reduces to

$$\partial_t \mathsf{B_r} + \mathbf{u} \cdot \nabla_h \mathsf{B_r} = 0 \,. \tag{4.55}$$

Toroidal flows are divergence free and confined to a spherical surface, i.e. there is no advection of toroidal field or upwelling of fluid flow.

Figure 4.15 allows a direct comparison of the secular variation prediction of the flows with the time–dependent model. All flows based on the tangential geostrophic assumption, flow 1 – 3, and the purely toroidal flow recover the secular variation and the jerks almost. Whereas, the drifting flow captures the secular variation roughly, without explaining short term variations. Figure C.1 in the appendix shows a comparison of the first 15 coefficients of the secular variation derived from different drifting flows.
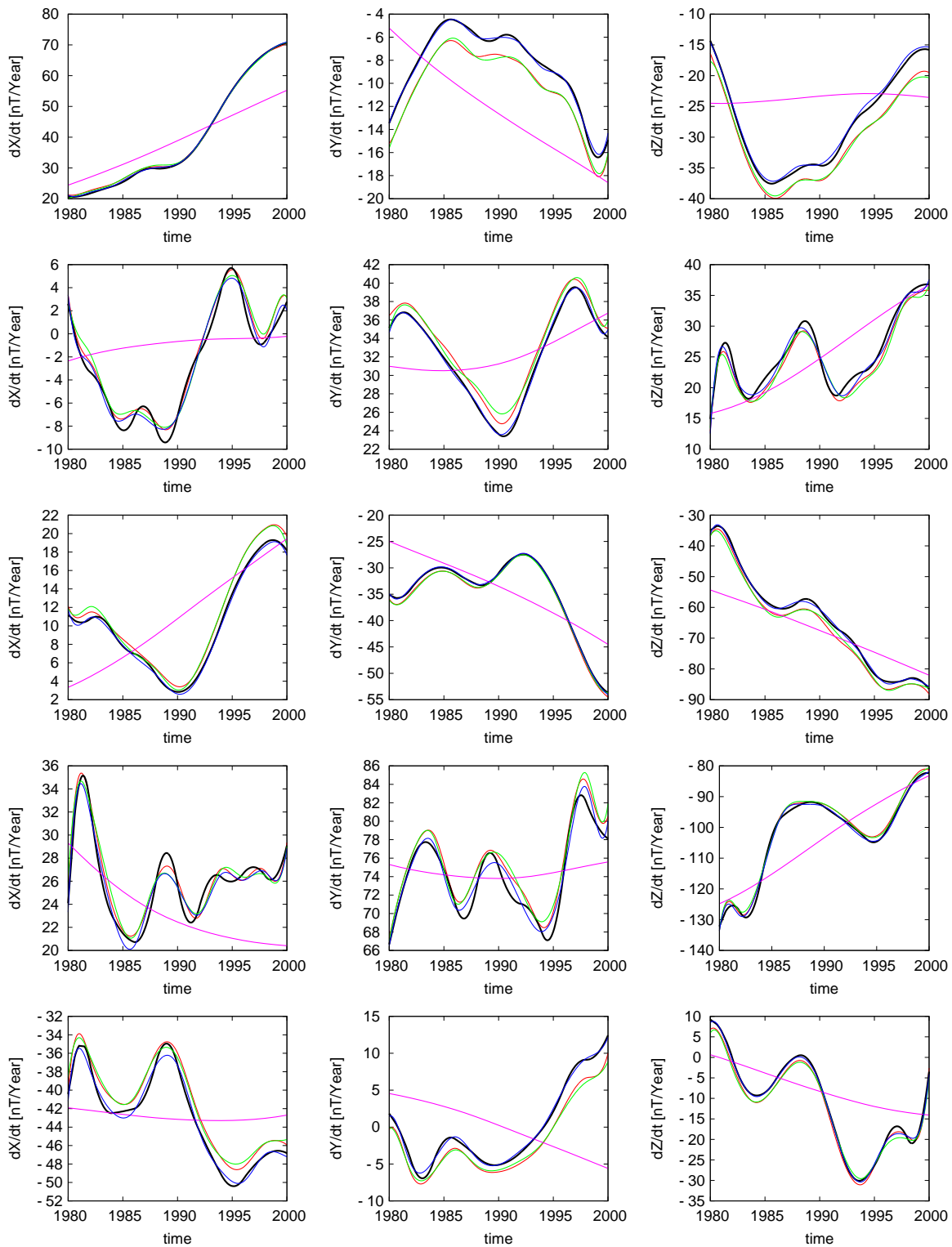
Figure 4.15: Comparison of modeled secular variation (solid black line) to the secular variation estimates at selected permanent observatories. Red curves are the prediction of flow 1, of flow 3 (green curves) and of the purely toroidal flow (blue curves). The pink curves are the prediction by the drifting flow (E1). From left to right: dX/dt, dY/dt, dZ/dt. From top to bottom: Resolute Bay (Canada), Niemegk (Germany), Newport (USA), MBour (Senegal), Pamatai (French Polynesian).
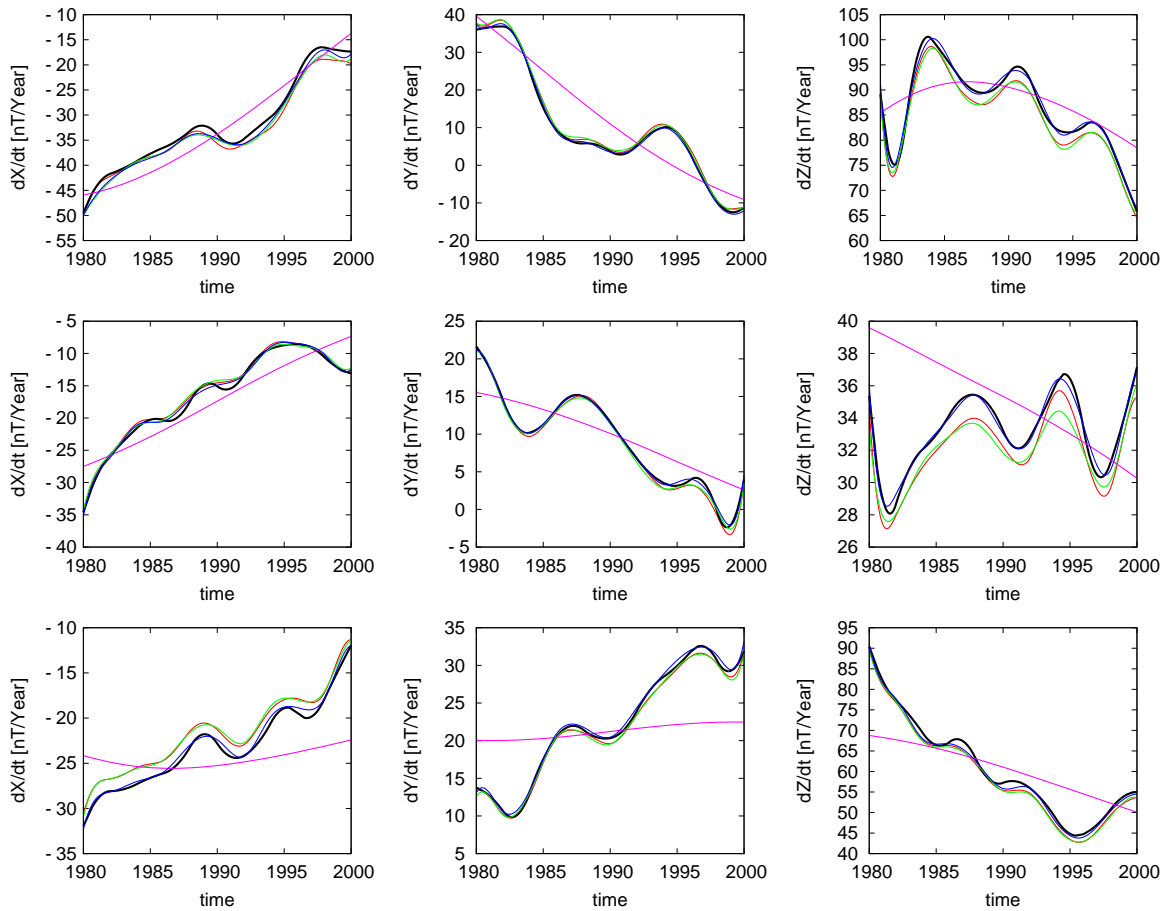
Figure 4.15: (*continued from previous page*) From top to bottom: Hermanus (South Africa), Eyrwell (New Zealand) and Scott Base (Antarctica).

4.2.5 Prediction of the decadal change of length of day

The Earth's rotation rate varies with periods ranging from a few days to at least a few thousand years. Several geophysical processes affecting the Earth's rotation rate: exchanges of angular momentum between solid Earth and either the atmosphere or oceans, tidal friction in the gravitational Earth–Moon–Sun system, seasonal exchange of angular momentum due to foliation and glaciation, or changes in the moment of inertia of the mantle due to post-glacial rebound. It is widely accepted that between core and mantle angular momentum is exchanged via a coupling mechanism [Hide & Dickey, 1991]. Because angular momentum is conserved an increase in the mantle rotation rate is associated with a slowing down of the core and vice versa.

Small differences between universal time (UT) and ephemeris time (ET) can be measured through astronomical observations, e. g., the time of lunar occultation of a star can be predicted to a high accuracy. Small changes in the Earth rotation rate cause discrepancies between the predicted time and the actual time, this time lag can directly be translated into a sidereal displacement angle ψ. ψ defines the relative position of the Earth to the stars. The first time derivative is the variation in the length of day (LOD)

$$\Lambda = \frac{d\psi}{dt}, \tag{4.56}$$

what is equivalent to the angular momentum

$$L = I \times \Lambda, \tag{4.57}$$

where I_M is the moment of inertia. The second time derivative is the observed torque on the mantle

$$\Gamma = I\frac{d^2\psi}{dt^2}, \tag{4.58}$$

Now the intention is to show how core surface motion can account for a small portion of Λ, when all other known contributions were removed. The basic idea is that the magnetic, inviscid, rotating fluid of the outer core interacts with solid lower most mantle via coupling. After rejecting viscous coupling as too weak [Rochester, 1984], three possible coupling mechanism remain. Mass anomalies and an aspherical shape of the core–mantle boundary region cause a non-radial component of gravity which might exchange angular momentum and generate a torque from the core to the mantle [Jault & Le Mouël, 1989]. These mass anomalies which directly translate into density heterogeneities are below seismic resolution, so this hypothesis cannot be tested directly. A further mechanism, which was explored in detail by Stix & Roberts [1984] and Holme [1998a,b, 2000], relies on the interaction of the induced currents in the lower most mantle with the magnetic field of the core to produce Lorentz torques. Another coupling mechanism was proposed by Hide [1969], which bases on assumptions about torques exerted by topographic coupling between core and mantle. Because of the high non–uniqueness of the torque calculation the form of coupling is still controversial.

The estimation of the core angular momentum is much simpler, it requires only that the surface flow matches the bulk flow on cylinders. The estimations follow directly from tangentially geostrophy of the flow.

$$\mathbf{u}_G = \mathbf{u}_\phi(s)\hat{\phi}$$

$$= -\mathbf{r} \times \nabla \left(\sum_{l=1}^{\infty} \sum_{m=0}^{l} t_l^m P_l^m \cos(\theta) \right)$$

It can be shown [Jault et al., 1988; Jackson et al., 1993] that the angular momentum as measured in the mantle rest frame is given by

$$L = \frac{8\pi}{15} c^4 \rho \left(t_1^0 + \frac{12}{7} t_3^0 \right) \tag{4.59}$$

and the change in the length of day can be predicted by

$$\Lambda = 1.138 \left(t_1^0 + \frac{12}{7} t_3^0 \right) [\text{ms}] . \tag{4.60}$$

The calculations by Jault et al. [1988] were made on the assumptions that all of the toroidal zonal flow was in the mode $\mathbf{u}_G$ by imposing symmetry about the equator on the calculations; requiring all terms $t_{2n}^0 = 0$ for $n \geq 1$. Jackson et al. [1993] relaxed this requirement, by postulate that angular momentum changes associated with the background convection and therefore the even toroidal zonal modes are small.

Figure 4.16 shows the change in the length of day deduced from astronomical measurement taken from Holme & de Viron [2005]. It also shows the predictions from the tangentially geostrophic flow without or with invoking torsional oscillation following from (4.60. The vertical offset is varied arbitrary to enable a clear distinction of the results for each flow type. The prediction from the drifting flow varies as the descending straight line and is not shown. Generally, the slope of Λ of the flow prediction is much steeper than the actual Λ, this agree well with [Holme & Olsen, 2005]. The green line shows the prediction of a flow, when the geostrophic constraint is relaxed.

Figure (4.17) depicts the averaged zonal velocities of the tangential geostrophic flow 1 and 2 at three dates. It is clearly visible that flow 2 shows significant variation in the zonal velocity and a equator-asymmetric state, which may explain the poor fit to the observed Λ (c.f. figure 4.17). The averaged zonal velocities of flow 1 are nearly symmetric to the equator.

4.3 Discussion and Conclusion

In this chapter the time–dependent model of the main field and its secular variation (developed in chapter 3) are treated as data, to invert the radial induction equation for different types of flows. Therefore, I have adopted the frozen flux hypothesis which ascribes the observed secular variation entirely to the effects of advection.
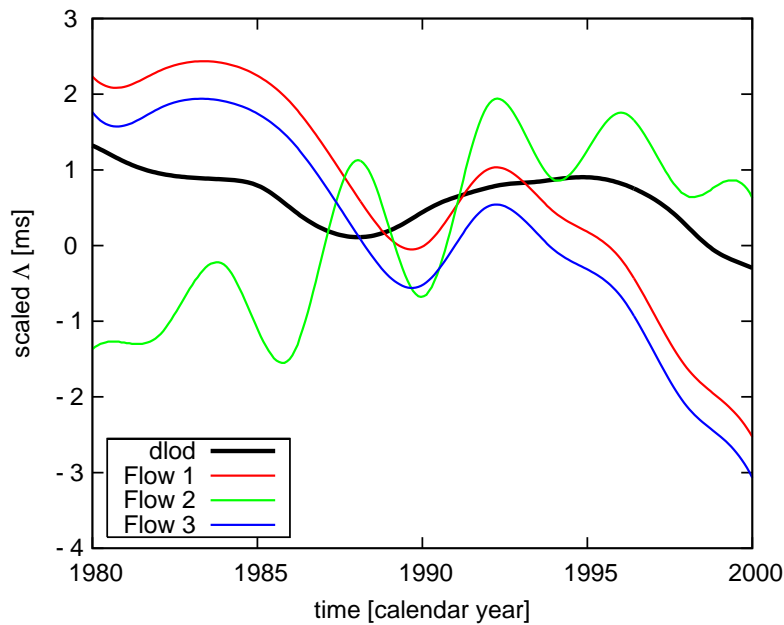
Figure 4.16: Comparison of Λ prediction. The black represent the Λ taken from Holme & de Viron [2005]. The colored curves are the predictions from the flows accordingly to the legend in the lower left corner.

The maps of steady flows and the drifting flow show less features than the maps of the flows 1 and 2, but all maps of all flows show a gyre south east of Africa and a feature underneath Labrador during the 20 years period.

It had been demonstrated that flows based on the tangential geostrophic assumption can explain almost of the observed secular variation and the change of the length of day. But, also a purely toroidal flow confined to a spherical surface, with no fluid upwelling and advection of toroidal field explains the secular variation equally well. The resolution analysis suggests that the poloidal component of flow 1 is mostly determined by the tangential geostrophic assumption. A relaxation of the tangential geostrophic constraint leads to a better fitting of the secular variation on one side, but on the other side the fit to Λ worsens (see table 4.2). This allow the conclusion that the poloidal component of the flow is less important for the generation of secular variation.

A second class of flow assumption as outlined in the first part of this chapter. Unlike the geostrophic flows, which are based on the dynamic description of the secular variation generation (i.e. Navier–Stokes equation), the steady flow assumption is a kinematic analysis of this. The steady flow assumption provides formal uniqueness for the inversion of the diffusion-less radial induction equation, but by definition a time–dependency of the solution is impossible. To introduce time–dependency to steady flow is therefore highly motivated. In fact, a steady flow in an azimuthally drifting reference frame improves the fit to the secular variation compared with single epoch steady flow. But it is still unable to explain
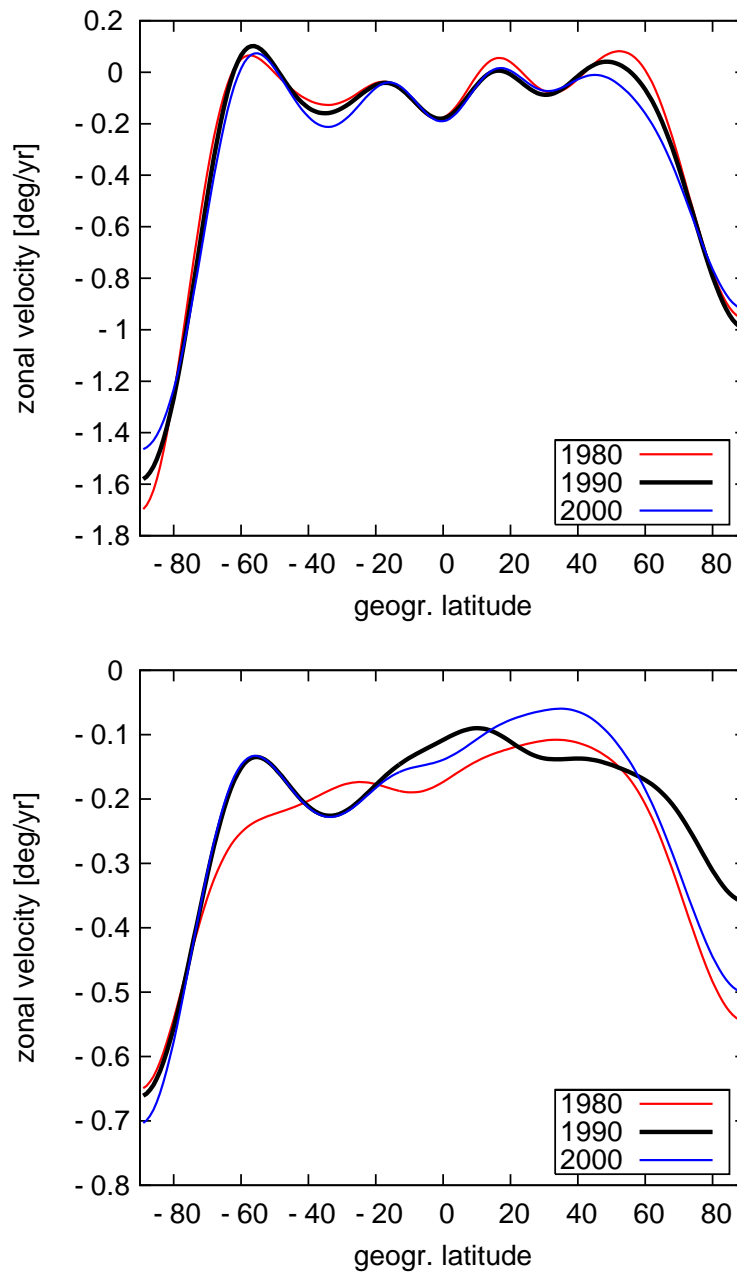
Figure 4.17: The zonal velocity profile for the epochs 1980, 1990, and 2000, derived from flow 1 (top) and flow 2 (bottom).

geomagnetic jerks in terms of generation by flows. Nevertheless, the drifting flow allows that the remaining signal might be explained by diffusion, whereas tangential geostrophic flows suggest that diffusion is unimportant.

The author is inclined to assume that geomagnetic jerks could be explained in terms of sudden flux expulsion, resulting in magnetic diffusion and a current in the lower most

mantle (see figure 4.9). The sudden appearance of currents may causes sudden acceleration or deceleration of the core, because a current system in the lower most mantle between regions of flux expulsion leads to an exchange of angular momentum form the core to the mantle. At the minute this is a speculation and needs to be proven and quantified.